Generic Performance Simulator of Spaceborne GNSS-Reflectometer for Land Applications

Hyuk Park, *Senior Member, IEEE*, Adriano Camps, *Fellow, IEEE*, Jordi Castellvi, and Jorge Muro

***Abstract*—Nowadays, the space missions employing the global navigation satellite system reflectometry (GNSS-R) are UK TDS-1, NASA CYGNSS, and the Chinese BuFeng-1A/B twin satellites, part of the first Chinese global navigation satellite system reflectometry (GNSS-R) satellite mission. They provide delay-Doppler map (DDM) measurements reflected from the land as well as the ocean. Using land reflected DDMs, several studies have been conducted to retrieve land geophysical parameters, such as soil moisture and biomass. Despite the clear dependence on these parameters, many other parameters impact the DDMs as well, such as topography, surface roughness, etc. The impact of these perturbing factors must be analyzed, and modeled in various conditions. This article presents a comprehensive end-to-end simulator that can generate synthetic DDMs reflected over land. It is an extension of a previously developed simulator validated for ocean applications. This simulator is very generic, and it includes numerous configurable parameters such as arbitrary scattering geometry (transmitter and receiver positions and speeds), arbitrary GPS and Galileo transmitted signals and frequencies, GNSS-R instrument antenna and receiver errors, as well as surface topography, roughness, soil moisture, vegetation cover, etc. The sensitivities of GNSS-R observables with respect to soil moisture and vegetation are obtained and compared to previous experimental results, and synthetic DDMs are compared and validated against TDS-1 ones.**

***Index Terms*—Global navigation satellite system reflectometry (GNSS-R), Simulator, scatterometry, soil moisture, TDS-1, vegetation.**

I. Introduction

THANKS to the successful operation of the spaceborne global navigation satellite system reflectometry (GNSS-R) instrument SGR-ReSI onboard TechDemoSat-1 [1] and CYGNSS [2] missions, many studies have been conducted to expand the applications of GNSS-R techniques for Earth observation. For ocean applications, such as wind speed and mean square slope, global data are routinely generated and distributed via data centers.[1] In addition to them, GNSS-R land applications are also being explored to measure new geophysical parameters, such as soil moisture, vegetation biomass, inland water bodies and wetlands, etc. [3]–[13]. Although the GNSS-R observables are sensitive to soil moisture, vegetation optical depth, and biomass, accurate retrievals from space are still a matter of research as many other effects have to be properly corrected [14].

The European Space Agency (ESA) funded the project "potential of Spaceborne GNSS-R for land applications" (ESA/ESTEC CONTRACT n. 4000120299/17/NL/AF/hh) to study the feasibility of spaceborne GNSS-R data to derive land parameters. The main objectives were to study are as follows.

1) Suitability of spaceborne GNSS-R to retrieve soil moisture and vegetation parameters.
2) Parameters that should be included in the model and their impact.
3) To study retrieval algorithms and the products using TDS-1 data. The first step for the project was to show the sensitivity of GNSS-R measurements to the variation of soil moisture and vegetation.

Although it has been shown that delay-Doppler map (DDM) descriptors can be used to retrieve geophysical parameters, the actual sensitivity to, for example, soil moisture was not properly known as different experiments had provided very different results (see discussion in Section V). Additionally, the DDM peak values are also affected by the elevation (incidence) angles, the receiving antenna pattern, the thermal noise level, as well as the topography and surface roughness of the reflecting surface among others. Therefore, in order to perform a comprehensive study including all these effects, an efficient and accurate end-to-end (E2E) simulator for GNSS-R over land is needed (e.g. [15]–[17]).

In this article, a generic E2E simulator is presented for the spaceborne GNSS-R land applications, titled "GARCA/GEROS-SIM4Land." It was originally developed for ocean applications [18], and it was progressively improved to include land effects [16]. This article describes its current status in detail. To date, a number of software tools have been developed to simulate the forward scattering of microwave

Manuscript received December 31, 2019; revised March 13, 2020 and May 5, 2020; accepted May 20, 2020. Date of publication June 5, 2020; date of current version June 18, 2020. This work was supported in part by the Spanish MCIU and EU ERDF Project (RTI2018-099008-B-C21) "Sensing with pioneering opportunistic techniques" and grant to "CommSensLab-UPC" Excellence Research Unit Maria de Maeztu (MINECO Grant MDM-2016-600), and in part by the ESA/ESTEC CONTRACT n. 4000120299/17/NL/AF/hh "Potential of Spaceborne GNSS-R for Land Applications." *(Corresponding author: Hyuk Park.)*

Hyuk Park is with the Castelldefels School of Telecommunications and Aerospace Engineering, Universitat Politècnica de Catalunya, 08034 Barcelona, Spain (e-mail: park.hyuk@upc.edu).

Adriano Camps and Jordi Castellvi are with the CommSensLab—María de Maeztu Unit, Universitat Politècnica de Catalunya, 08034 Barcelona, Spain (e-mail: camps@tsc.upc.edu; jordi.castellvi@tsc.upc.edu).

Jorge Muro is with the School of Industrial, Aerospace and Audiovisual Engineering of Terrasa, Universitat Politècnica de Catalunya, 08034 Barcelona, Spain (e-mail: axonn_jm@hotmail.com).

Digital Object Identifier 10.1109/JSTARS.2020.3000391

[1]Online. [Available]: http://merrbys.co.uk/; https://podaac.jpl.nasa.gov/dataset/CYGNSS_L2_V2.1

signals over land, some of them including the effect of surface roughness, vegetation cover, and even topography. The main features of this simulator reside in its generic approach, including numerous tunable input parameters from the signal frequency, and structure (GPS or Galileo and type of transmitted codes), to the receiver and antennas imperfections, as well as surface and vegetation parameters, including topography that impact the shape and values of the DDM. The simulator has been validated with several TDS-1 data tracks. It is important to highlight that the approach followed avoids as much as possible sophisticated numerical electromagnetic methods (e.g. for vegetation scattering [19]) that will be very time-consuming. Additionally, in practice these methods also prove to be quite difficult to use because in general, it is either impossible to know the values of the input parameters, or because these parameters could be adjusted to many sets of values to fit the real data, but may lack the capability to predict the GNSS-R observables in other conditions.

The article is structured as follows. In Section I, the structure and the main algorithms are described. The operation and the example results are presented in Section II. The simulator has been validated using the TDS-1 data, and some validation results are shown in Section III. One of the advantages of the simulator is its capability to conduct sensitivity analyses with respect to selected parameters. In Section IV, sensitivity results to several parameters are presented. Finally, the main conclusion is presented in Section V.

II. Simulator Structure and Algorithms

The simulator has been developed and implemented efficiently by using the heritage of spaceborne GNSS-R ocean simulator. The CommSensLab in UPC-BarcelonaTech developed the E2E simulator, "GARCA/GEROS-SIM M2" as participating in the PARIS-IoD and GEROS-ISS projects [20]. The land simulator uses many parts of the predecessor, e.g., the geometry, the DDM generation, and the instrument modules which were described in detail in [18], and are just summarized later. The main module to be replaced is the scene generation module which computes the land reflection coefficients corresponding to the observed scene geophysical parameters in each facet in which the surface topography is discretized, e.g., soil moisture, surface roughness, and vegetation cover/land use. The computed reflection coefficients are further processed to generate the reflection intensities which are then observed by the GNSS-R instrument according to the scattering scenario. In this section, the structure of the simulator is described with the details of each functional module.

A. Structure of the Simulator

Fig. 1. shows the structure of the GEROS SIM-4Land simulator. It consists of three main modules: geometry, scene generation, and DDM generation module. These three modules compute the intermediate and final data of the simulation according to the input parameters. The module outputs are used for the inputs of the other module.

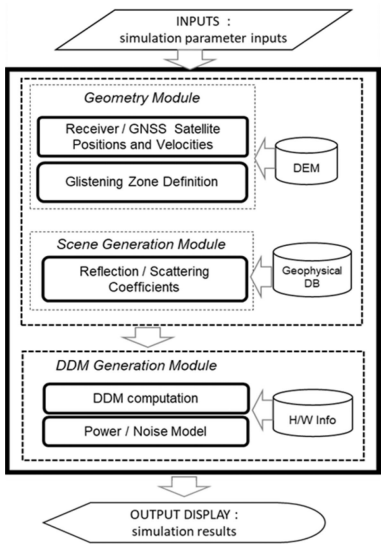

Fig. 1. Structure of GARCA/GEROS-SIM4Land.

GEROS/GARCA SIM also uses a geophysical database that includes among others a global digital elevation model (DEM), soil moisture, vegetation optical depth, surface roughness maps, etc. The instrument information used includes the delay and Doppler bins resolution size and width, receiver gain and frequency response, system noise temperature, and antenna pattern (including beamforming).

Generally, the structure is similar to the ocean GNSS-R simulator [18], except for the scene generation module which now computes the signal reflections over land.

The simulator has two modes: static/parameter sweep mode, and orbit progressing/Inhomogeneous mode. The static mode simulates the DDM varying only one single input parameter, holding the other parameters as constant. This mode is efficient to study the impact of that parameter on the DDM. The orbit progressing mode simulates the DDM according to the actual instrument and orbit as the spacecraft moves on each epoch. It is convenient to simulate the actual spaceborne GNSS-R instrument like TDS-1. More details of the two modes are given in Section III.

B. Geometry Module

The Geometry module first defines the spaceborne GNSS-R observation geometry according to the user input parameters. The states (position and velocity) of the GNSS transmitting and receiving satellites are computed in the Earth reference frame, Earth-centered Earth-fixed or ECEF. In the static mode, the position of the specular reflection point is provided by the user as an input. For the orbit progressing mode, the specular point is provided from the metadata, such as TDS-1 NetCDF file from.[2]

After this, the glistening zone (field of view) is defined. The area around the specular reflection point is selected considering the observation geometry and the number and size of delay/Doppler bin. For example, the FOV size of 200 km is

[2]Online. [Available]: http://merrbys.co.uk/

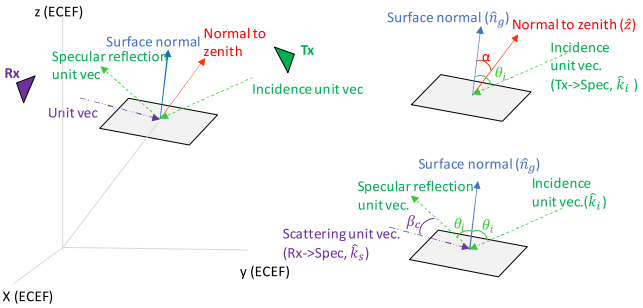

Fig. 2. Reflection/scattering geometry of the surface facet. The interested reader is referred to [21] for a detailed formulation of the equations to compute the above vectors and angles.

large enough for an orbital height of ∼700 km. It contains the delay of the more than 50 C/A chips and ±4 kHz of the Doppler spread. The size of FOV is a user-defined input parameter to be adjusted considering the computing time.

Once the area of the FOV/Glistening zone is defined, the information of the land facets is read from a global DEM. In this simulation, ETOPO1 is used, which has 1 arc-min resolution (maximum distance at the equator ∼1.8 km). It is possible to use a different DEM with higher resolution by modifying the simulator setup. However, computation time increases significantly as the number of facets increases, and during the validation process it was found that this resolution reproduced correctly the dynamic range of the variability of the peak power of the DDM. It must be noted that other input parameters such as the surface soil roughness cannot be determined accurately, and have a large impact in the dynamic range as well.

From the positions of facets, the vectors describing the geometry of reflection and scattering are defined as shown in Fig. 2.

The following unit vectors and the angles are calculated.

1) Normal vector to the zenith $\hat{z}$.
2) Surface normal vector $\hat{n}_g$.
3) Incidence and specular reflection unit vectors $\hat{k}_i$.
4) Scattering unit vector: the direction of the facet from the receiver positions $\hat{k}_s$.
5) The angle between the surface normal and zenith vector α.
6) Local incidence angle θ_i: the angle between the surface normal and incidence vectors.
7) The angle between the reflection and scattering vectors β_c.

Those vectors and angles are used for the computations of the reflection and scattering coefficients in the scene generation module.

C. Scene Generation Module: Reflection and Scattering Corresponding to the Land Cover

The scene generation module computes the reflection and scattering coefficients considering the land surface conditions, which are land cover types, geophysical values, and observation geometry. The attenuation by the vegetation is also included. The output of the module is the reflection/scattering scene which is collected by the receiver antenna. In the simulation, this scene is reformatted in the delay/Doppler domain and convolved with the woodward ambiguity function (WAF).

The first step of scene generation is the computation of the Fresnel reflection coefficient according to the observation geometry and the values of the geophysical parameters on the facets. The vectors and the angles of observation geometry are provided from the output of the geometry module. The geophysical parameters are provided from the user inputs (static mode) or read from a database (orbit progressing mode). Then, the reflection coefficients in linear polarization are calculated as

$$\rho_{VV} = \frac{\varepsilon\cos\theta_i - \sqrt{\varepsilon - \sin^2\theta_i}}{\varepsilon\cos\theta_i + \sqrt{\varepsilon - \sin^2\theta_i}},$$
$$\rho_{HH} = \frac{\cos\theta_i - \sqrt{\varepsilon - \sin^2\theta_i}}{\cos\theta_i + \sqrt{\varepsilon - \sin^2\theta_i}} \quad (1)$$

where ε is dielectric constant of the facet.

The circular polarizations are calculated from the linear polarization reflection coefficients as

$$\rho_{\mathrm{RL}} = \rho_{\mathrm{LR}} = \frac{1}{2}\left[(\rho_{\mathrm{VV}} - \rho_{\mathrm{HH}}) + \mathrm{j}\,(\rho_{\mathrm{VH}} + \rho_{\mathrm{HV}})\right]$$
$$\rho_{\mathrm{RR}} = \rho_{\mathrm{LL}} = \frac{1}{2}\left[(\rho_{\mathrm{VV}} + \rho_{\mathrm{HH}}) + \mathrm{j}\,(\rho_{\mathrm{HV}} + \rho_{\mathrm{VH}})\right]. \quad (2)$$

The power reflection coefficient including surface roughness in is modeled as

$$\Gamma_{RE,\mathrm{eff}} = |\rho_{RL}|^2 e^{-4k^2\sigma_h^2\cos^2\theta_i} \quad (3)$$

where k $(= 2\pi/\lambda)$ is wavenumber, λ is electromagnetic wavelength, and σ_h denotes the surface rms height.

The linear pol reflection coefficients ρ_{vv}, ρ_{HH} are computed based on the SAIRPS radio transfer model [22]. In the SAIRPS RTM, the average reflection coefficients of the composite land covers are computed based on the portion of the land cover type, using the geophysical database constructed for SAIRP RTM, e.g., mixed soil (including vegetation), sand desert, no sand desert, frozen soil, snow soil, urban soil, etc.

Once the reflection/scattering coefficients of the facets are computed, they are reformatted from the spatial domain to the delay/Doppler domain. Each facet has its own delay and Doppler-frequency according to the observation geometry taking into account the surface height. Therefore, the values of the reflection/scattering coefficients of the facets are assigned and mapped onto their delay-Doppler coordinates. These values are finally interpolated on a regular delay/Doppler grid in order to be convolved with the WAF and obtain the DDM.

The modelling of the vegetation effects could follow a very complex approach such as in [21], [23], and [24], but the problem is finding the right input parameters to run the model. Therefore, a more pragmatic approach has been followed, inspired in the τ-ω model used in microwave radiometry at *L*-band [25]. Assuming negligible scattering effects, the vegetation impact is applied as an attenuation of the power, as shown in Fig. 3.

The power attenuation dependence on the biomass [see Fig. 3(a)] is modeled based on the results of [24], [26], and it was provided by University La Sapienza during the project. Considering the global map and database of VOD is more available than the biomass, the simulator utilizes the VOD as an

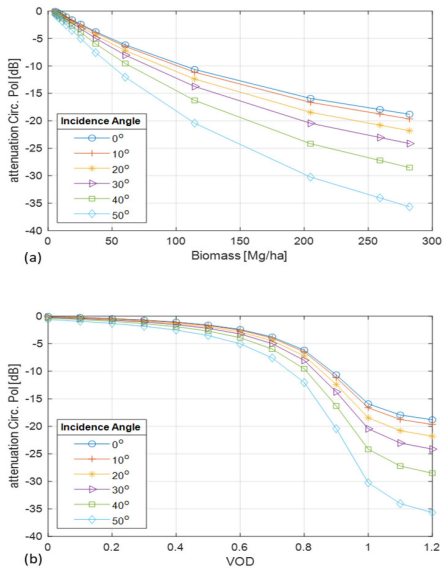

Fig. 3. Attenuation of the reflected signal power by vegetation. (a) With respect to Biomass (parametric model provided by Tor Vergata University of Rome during the project). (b) With respect to VOD.

input. The VOD is then converted to biomass using the model in [27], and the attenuation of the received power is then obtained from Fig. 3(b).

D. DDM Generation Module

The power of received signals from the GNSS-R instrument P_r have two components: coherent and incoherent components

$$P_r = P_r^{coh} + P_r^{inc}. \tag{4}$$

Many studies have recently reported the coherent scattering of GNSS-R over land [28]–[30]. For the simulator, a widely used simple coherent scattering model [31] is used considering the efficiency. The coherent component in *pq* polarization is modeled as

$$P_r^{\text{coh}} = \frac{P_T \lambda^2 G_T G_R}{(4\pi)^2 (R_t + R_r)^2} \cdot |\Gamma_{pq}(\theta_{\text{inc}})|^2 \tag{5}$$

where R_t and R_r are the distance from the reflection point to the transmitter and the receiver satellites, respectively; P_T is the GNSS satellite transmitted power; G_T and G_R are the antenna gains of the transmitter and the receiver, respectively.

The incoherent component is modeled as

$$P_r^{inc} = \frac{P_T \cdot \lambda^2}{(4\pi)^2} \int\int_A \frac{G_T G_R \sigma^0 |\chi(\tau - \tau', f - f')|^2 \Lambda^2(\tau - \tau') S^2(f - f')}{R_t^2 \cdot R_r^2} d\vec{r'} \approx \frac{P_T \lambda^2 G_T G_R \sigma^0 A_{\text{eff}}}{(4\pi)^3 R_t^2 R_r^2} \tag{6}$$

where A_{eff} is the area of the facet and σ^0 is scattering coefficient (or normalized radar cross section); WAF is denoted by $\chi(\tau, f) = \Lambda(\tau) S(f)$.

For the computation efficiency, the integral form can be computed as 2D convolution of the WAF $|\chi(\tau, f)|^2$ and the reflected power [32]

$$\text{DDM}(\tau, \text{f}_\text{D}) = |\chi(\tau, f)|^2 * * P_r(\tau, f). \tag{7}$$

Then, the power of the received signal is estimated. If the power calibration method of the instrument is unknown, an effective way to estimate the received power is based on the nominal valued of the GNSS signal power on the Earth's surface assuming a unity receiver antenna gain ($G_R = 1$)

$$P_{\text{nominal}} = \frac{P_T \lambda^2 G_T}{(4\pi)^2 (R_t)^2}. \tag{8}$$

The nominal powers of various GNSS signals are listed in [33]. For example, the nominal power of GPS C/A signal is -155.5 dBW. It means that we can replace the terms in DDM power model in (5) and (6) with -155.5 dBW. Since in the LEO case ($R_t \gg R_r$) and $(R_t + R_r)^2 \approx (R_t)^2$, the received power can be estimated by substituting the received antenna gain G_R, the distance between the facet and the receiver satellite R_r, and the reflection/scattering term Γ_{pq} and σ^0. Then the coherent component (5) becomes (linear units)

$$\begin{aligned} P_r^{\text{coh}} &= P_{\text{nominal}} \cdot |\Gamma_{pq}(\theta_{\text{inc}})|^2 \\ &= 10^{-155.5/10} \cdot |\Gamma_{pq}(\theta_{\text{inc}})|^2 \quad [\text{W}]. \end{aligned} \tag{9}$$

Receiver antenna gain, including arrays with beam steering, and possibly pointing errors are included afterward. The coherent components are included only for the specular reflection condition satisfying the equal incidence and reflection angles to the surface normal, i.e. $\beta_c = 0$ in Fig. 2. However, in reality, a perfect specular reflection does not exist, as an infinitely narrow forward-scattering beam would only exist if the reflection takes place over a perfectly flat (roughness much smaller than the wavelength), and over an infinitely large facet (much larger than the first Fresnel zone).

To properly apply the tolerance, facet size, which is larger than the first Fresnel zone is considered, because the coherent reflection is basically coming from that zone [29], [34]. For the spaceborne GNSS-R case, the diameter of the average Fresnel zone is around 700 m for the receiver altitude of 700 km [28].

In this simulator, the facet size is larger than the diameter of the first Fresnel zone, e.g., 1 arc-min DEM ($\sim$1.8 km facet size). For the validation test suing TDS-1 scenario, the width of the scattering pattern of 0.1° around the forward scattering direction has been used [35].

For the incoherent components, it can be simplified using nominal power

$$P_r^{\text{inc}} = P_{\text{nominal}} \frac{\sigma^0 A_{\text{eff}}}{4\pi R_r^2}. \tag{10}$$

For the calculation of σ^0, two effects of surface roughness and geometry are introduced. First, the surface roughness introduced as the effect of attenuation and scattering (widening of the reflected ray). By using the formula of these two effects in [28],

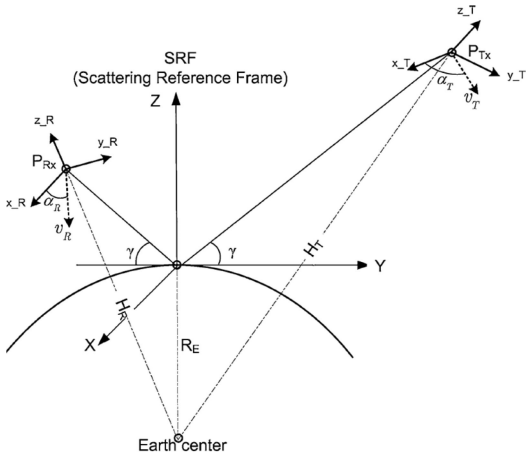

Fig. 4. Observation geometry for the static mode of the simulation.

[29], and [36]

$$\sigma^0 = \frac{|\rho_{RL}|^2}{s^2} \exp\left[-\left(\frac{\beta_c}{s}\right)^2\right] \tag{11}$$

where s is rms surface slope. For an isotropically rough surface with a Gaussian correlation function, s is related to the rms height σ_h by the correlation length [35]. The values of s range typically from 0.1 to 0.17 overland [35]. The term of division by s^2 apply the attenuation by the surface roughness, and the exponential term introduced the scattering. The scattering of the facets in the non-specular points ($\beta_c \neq 0$) is accounted for by the exponential term in (11). This scattering becomes wider as the surface roughness term s increases.

After obtaining the coherent and incoherent power, the final received power can be computed by applying the vegetation attenuation shown in Fig. 3.

Last, thermal and speckle noises are introduced in the computed DDMs, as described in [18]. The interested reader is referred to this publication for further details.

III. Operation of GEROS-SIM4Land

The simulator has two operation modes: static/parameter sweep mode and orbit progressing/inhomogeneous mode.

A. Static/Parameter Sweep Simulation

The static mode simulates the DDM as varying a single input parameter, holding the other parameters as constant. This mode is efficient to study the impact of a single parameter on the DDM. In this case, the observation geometry is defined in the scattering reference frame shown in Fig. 4. The definition of the scattering reference frame is explained in [37].

In the static mode, the position of the specular reflection point is set as user input. Other user inputs for this mode are the receiver orbital height ($H_R - R_E$), the elevation angle (γ), the azimuths of the *Tx* and the *Rx* satellites moving (α_T, α_R). In order to apply the topographic effect, the specular point should be defined on the Earth's surface as (latitude, longitude) to introduce the DEM. With the specular point, the azimuth of the *Tx-Sp-Rx* line (*y*-axis of Scattering Reference Frame) is also user-defined. The azimuth angle is measured counterclockwise from the meridian. With the user input parameters earlier, the observation geometry with the corresponding parameter can be computed by the geometry module of the simulator.

In the static/parameter sweep mode, the DEM (ETOPO1) of the facet is used for the topography, and additionally the geophysical parameters impacting the DDM are set by user input. These are the land cover type, soil moisture, vegetation optical depth, and surface roughness. It means that the simulator can generate DDM with the change of geophysical parameters, i.e., parameter-sweep. In this case, the conditions of geophysical parameter of the facets are set to be constant over the glistening zone, in other words homogeneous FOV. An example of the simulation results of static mode is shown in Fig. 5. Although this is not the real situation of the FOV, this mode is convenient to simulate the sensitivity of single parameter holding the other parameters constant. The inhomogeneous FOV simulation mode is more realistic for the actual situation, discussed in the following section.

For the computation time of this mode, it simulates a snapshot DDM such as the result of Fig. 5 in 4 s on average under the computation resources of 3.2 GHz CPU with 16 GB memory.

B. Orbit Progressing/Inhomogeneous FOV Simulation

The orbit progressing mode for inhomogeneous FOV simulates the DDM according to the actual orbit progress on each epoch. This mode is convenient to simulate the actual spaceborne GNSS-R instrument like TDS-1. In this case, the *Tx* and *Rx* states (positions and velocities) are inputs of the simulation. It means that the metadata of TDS-1 (or any space-borne GNSS-R instrument) can be directly imported to the simulation inputs. The specular point information in the metadata could be used to efficiently define the FOV.

The geophysical data are also read from the database. Once the positions of facets are defined, correspondingly the geophysical data are read from the global DB. For the DB, the simulator uses the one constructed during the SAIRPS RTM development. Accordingly, the FOV of the orbit progressing mode simulates the DDM on the condition of inhomogeneous geophysical parameters. This mode is useful to compare to the TDS-1 data, and to simulate any future spaceborne GNSS-R mission. Fig. 6 shows the simulation results of one snapshot in the case study of the orbit progressing mode, described in the following section.

This mode takes a bit more time compared to the static mode because of the access to the DB in a disk drive. On average, it takes 7.5 s for the generation of DDM in Fig. 6 under the same resources in the static mode with solid-state drive.

IV. Study on Inhomogeneous FOV as Intercomparison With Measured TDS-1 Data

This section presents the results for inhomogeneous FOV of the orbit progressing mode, which has been conducted at the validation of the simulator. The simulations were performed by finding interesting points on the L1b Catalogue of TDS-1

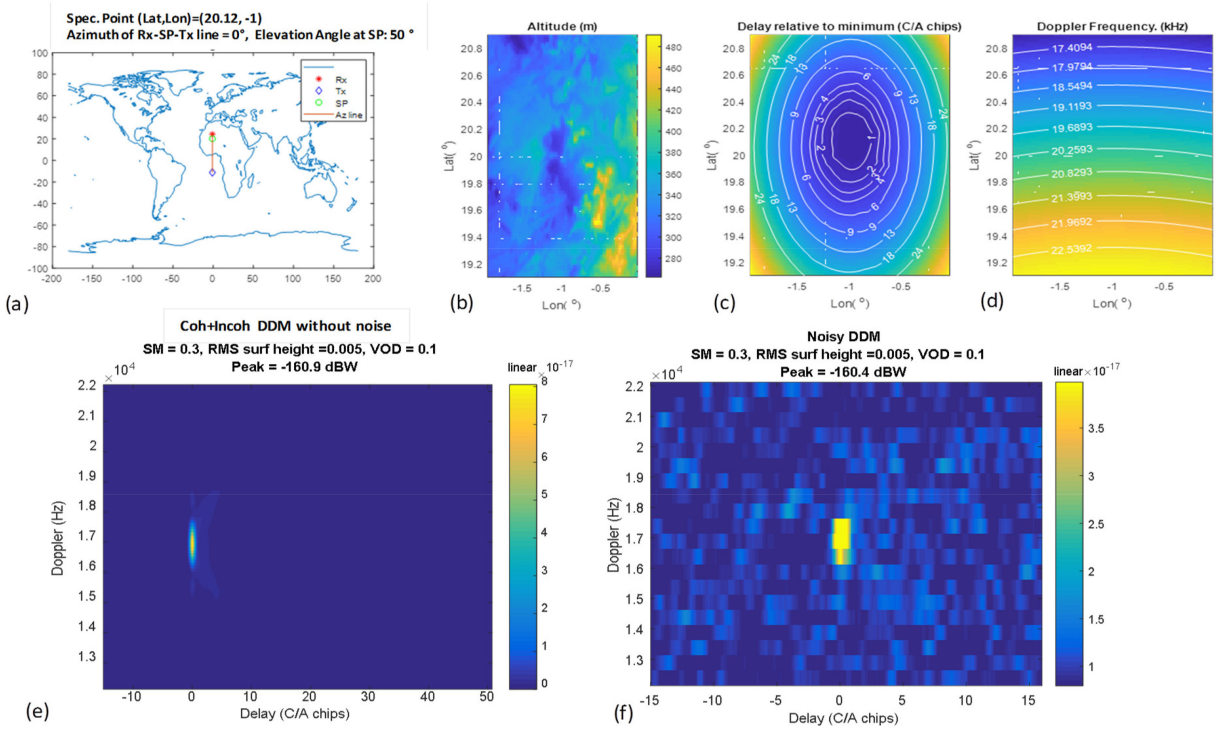

Fig. 5. Example of static mode simulation (a) Observation geometry. (b) Altitude. (c) ISO-delay. (d) ISO-Doppler of FOV. (e) Noise-free. (f) Noisy DDMs.

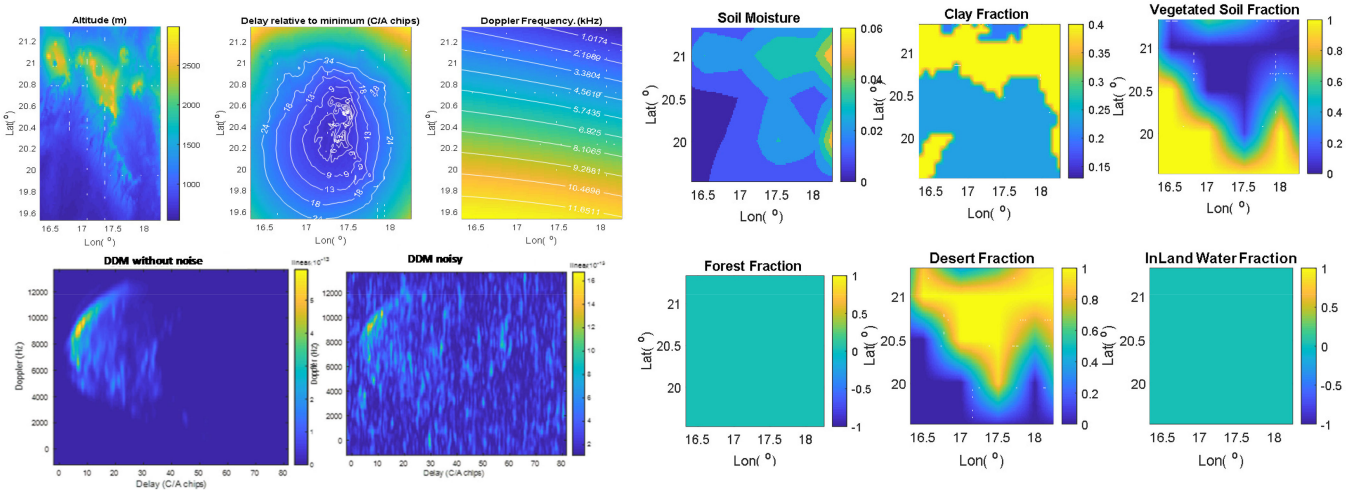

Fig. 6. Example of the orbit progressing mode simulation: (first row from left) altitude, ISO-delay, and ISO-Doppler, SM, clay fraction, and vegetation fraction of FOV; (second row from left) noise-free DDM, noisy DDM, forest fraction, desert fraction, and in-land water fraction.

with different land conditions. After selecting these regions, the corresponding L1b metadata files were read to get all the information.

A. *Case 1: Tunisia, Dry, and Flat Region*

This location was chosen mainly for its high desert fraction. This specific part of Tunisia is quite flat and mostly on a desert, as well as having no mountains or in-land water zones, which makes it ideal to see how the simulator performs. From TDS-1 data, the time chosen is July 4, 2017, at H00, satellite number 93. The track of the TDS-1 is shown in Fig. 7. From the track, a simulation of 40 snapshots was conducted on this location.

All the DDMs on this desert part have very low peak values due to the geophysical conditions. Fig. 8 shows three DDMs from the simulation results and the corresponding TDS-1 measurements.

Fig. 9 shows the DDM peak values of case 1. The simulated DDM peak power is quite weak due to dry condition, which is around -170 dBW. Both the simulation and real DDM peaks

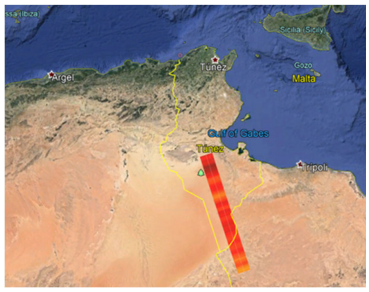

Fig. 7. Track of the TDS-1 in case 1: Tunisia, dray, and flat.

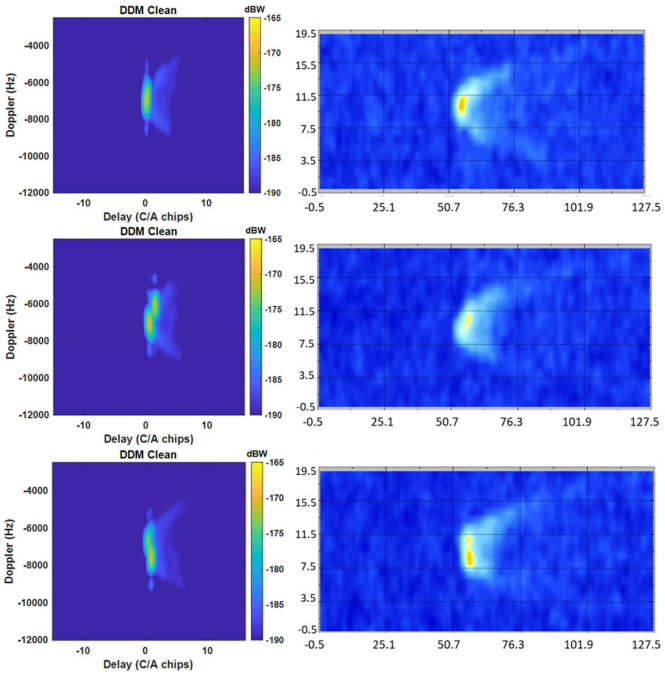

Fig. 8. Simulated DDMs in dBW (left panel) and TDS-1 DDMs in linear scale (right panel) for Tunisia (case 1) at 19 s (top), 26 s (middle), 29 s (bottom).

have similar trends, being somehow different in the middle part. There is also a peak value on the final part of the DDM peak plot, which corresponds to flat ground.

B. Case 2: Chad, Dry Soil, and High Topography Variation

The next location of interest is the northern part of the Chad region. This location is interesting due to its dry land, high desert fraction, but it is very different from Tunisia because as seen in Fig. 10, it has a high topographic complexity on its Northern part. The date of this TDS-1 track was November 29, 2016, satellite number 83. There were two sets of data with different time tracks. Within these sets, the satellite tracks are from 747 to 857 on the local data file and from 269 to 379 on the metadata file. A simulation was conducted for 40 snapshots along the track.

Fig. 11 shows the DDM peak values of case 2. The trend of simulation peaks follows well the measured one. From all the 40 simulation results, three DDMs in the interesting region are shown: one on the mountain area (up to around 5 s), another on

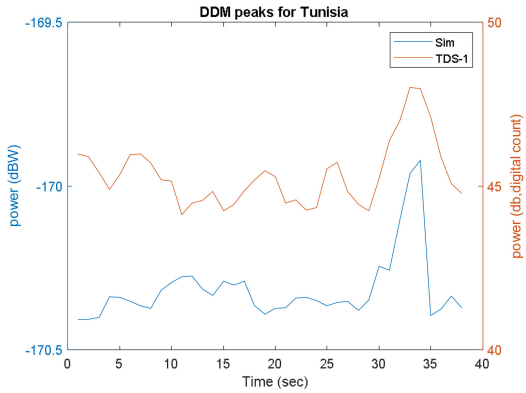

Fig. 9. DDM peak values of case 1: simulated power (blue line) and TDS-1 digital count (red line).

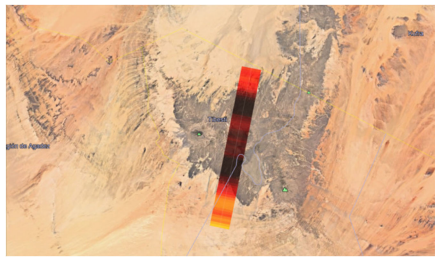

Fig. 10. Track of the TDS-1 in case 2: Chad, dry and high altitude variation

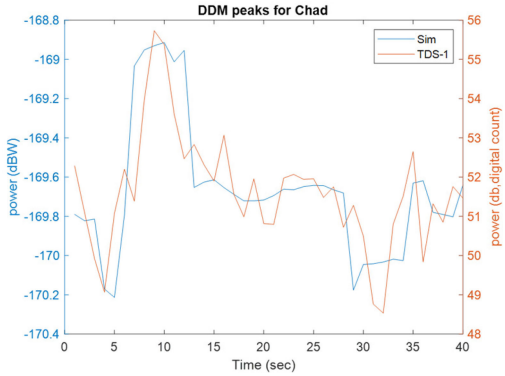

Fig. 11. DDM peak values of case 2: simulated power (blue line) and TDS-1 digital count (red line).

the high peak (around 11 s), and another in the more desert area (around 31).

1) *High topography variation*: The first low part of the graph corresponds to the mountain part of Chad, and thus the reflectivity of the dry, stone-like mountain environment is not very high, giving very low values DDM peaks. An example of the DDMs in this part is shown in Fig. 12 (top).
2) *High reflectivity peak value*: The high peak corresponds to an area that still is in a 500 m height, but there are not so many topographical complexities, it is when the mountain starts to go down and the surface becomes flat. An example of the DDMs in this part is shown in Fig. 12 (middle).

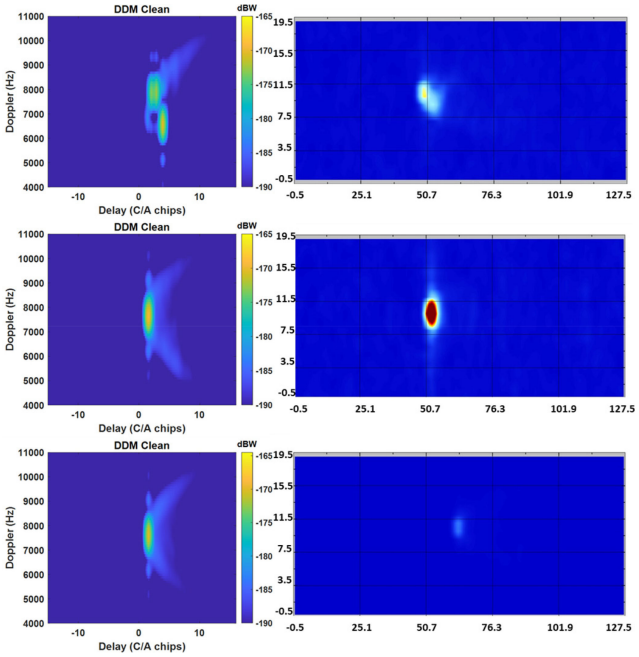

Fig. 12. Simulated DDMs in dBW (left panel) and TDS-1 DDMs in linear scale (right panel) for Chad (case 2) at 5 s (top), 10 s (middle), 30 s (bottom).

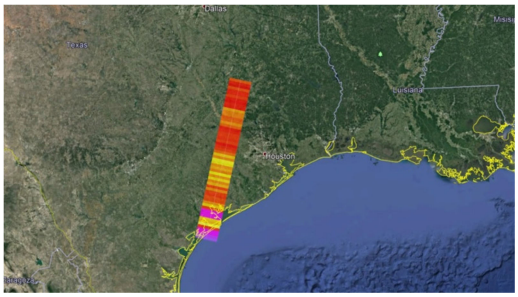

Fig. 13. Track of the TDS-1 in case 3: Texas, low vegetation, and coast.

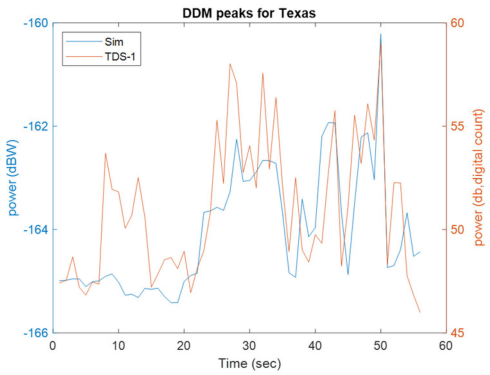

Fig. 14. DDM peak values of case 3: simulated power (blue line) and TDS-1 digital count (red line).

3) *Desert area*: In the desert area, it gives quite low powers overall. An example of the DDMs in this part is shown in Fig. 12 (bottom).

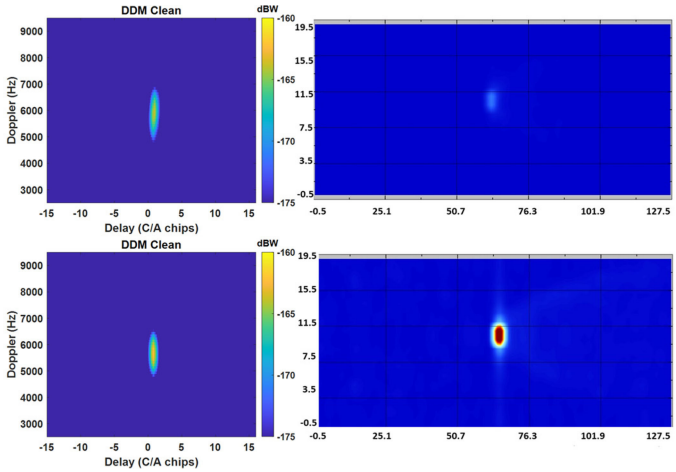

Fig. 15. Simulated DDMs in dBW (left panel) and TDS-1 DDMs in linear scale (right panel) for Texas (Case 3) from a vegetated area at 20 s (top), and the coastal area at 51 s (bottom).

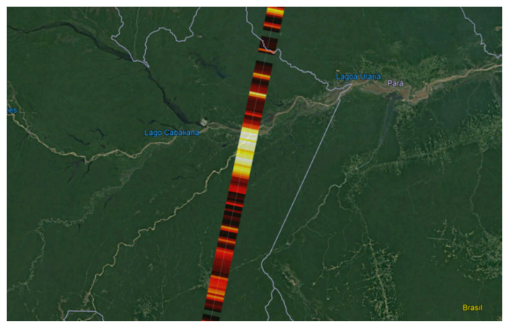

Fig. 16. Track of the TDS-1 in case 4: Amazon, high vegetation, and inland water.

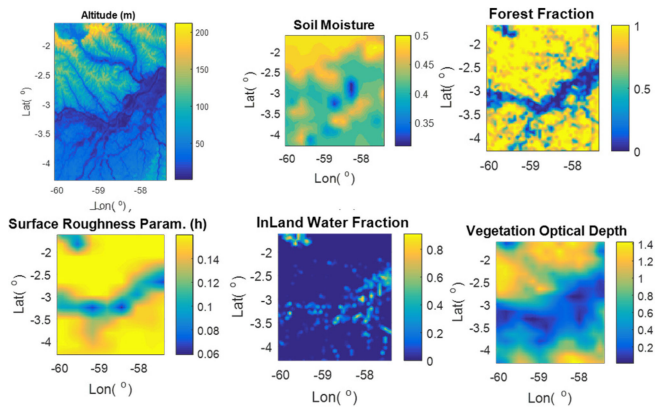

Fig. 17. Geophysical parameters of FOV in case 4.

C. Case 3: Texas, Low Vegetation, and Coastal Region

This location was chosen considering the low amount of vegetation, which is not so low as to be a desert, but not so high as to be a forest-like Amazon. The soil moisture is also higher than in cases 1 and 2. Also, the coastal area can be simulated in this case. The selected day is July 3, 2017, at H18, satellite number 160. A simulation of 56 snapshots was performed in this area. The satellite track of this case is shown in Fig. 13.

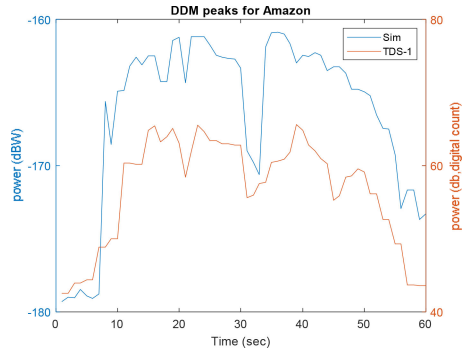

Fig. 18. DDM peak values of case 4: Simulated power (blue line) and TDS-1 digital count (red line).

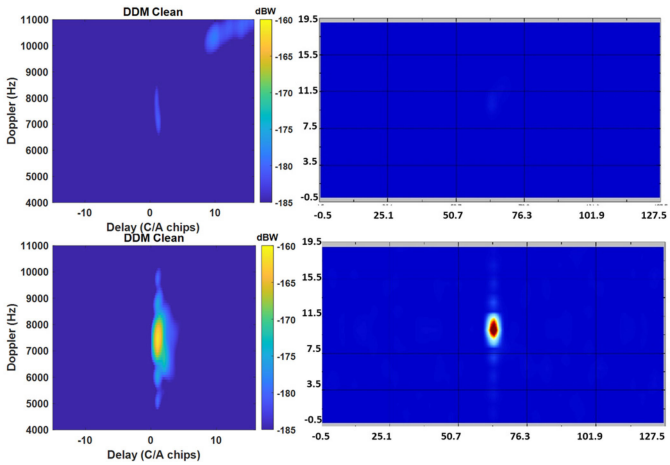

Fig. 19. Simulated and TDS-1 DDMs for Amazon at 4 s; The reflected signal is m Simulated DDMs in dBW (left panel) and TDS-1 DDMs in linear scale (right panel) for Amazon (case 4) from a vegetated area at 4 s (top), and the in-land water area at 22 s (bottom).

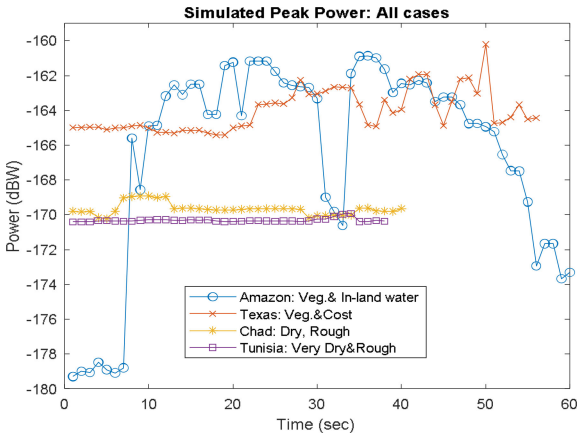

Fig. 20. DDM peak values of all four cases.

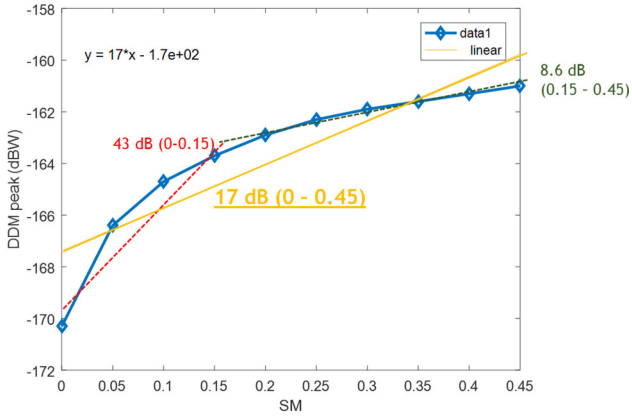

Fig. 21. DDM peak values with respect to the SM. The other input parameters are held as the RMS surface height of 1 cm, the VOD of 0.001.

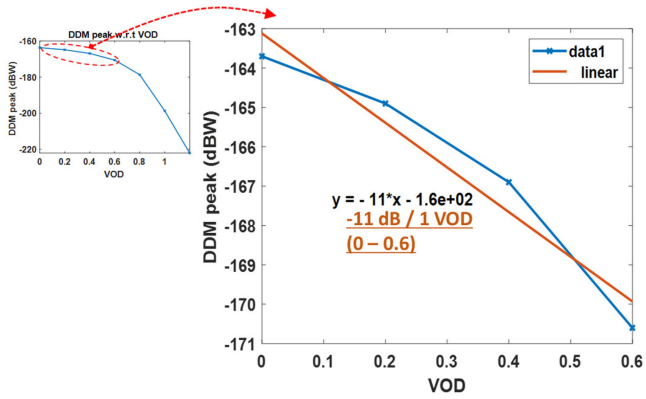

Fig. 22. DDM peak values with respect to the VOD.

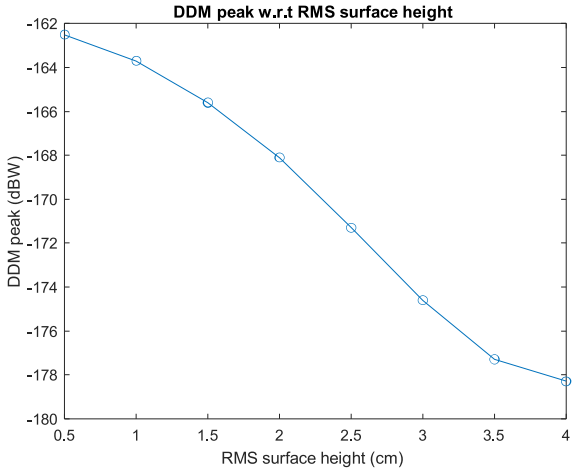

Fig. 23. DDM peak values with respect to the RMS surface height.

As it can be seen in Fig. 14, both the simulated and the measured DDM peak curves are very similar. The first part is vegetated soil exhibiting a low reflected power, and the last part is a coastal area showing the high reflected power because of the presence of water bodies.

All the DDMs over this area had a pretty similar shape (concentrated on the specular point), and there was not a lot of variety due to flat topography in this region. The roughness of the soil together with the medium vegetation generates a medium level of reflectivity (~ -165 dBW). The coast part

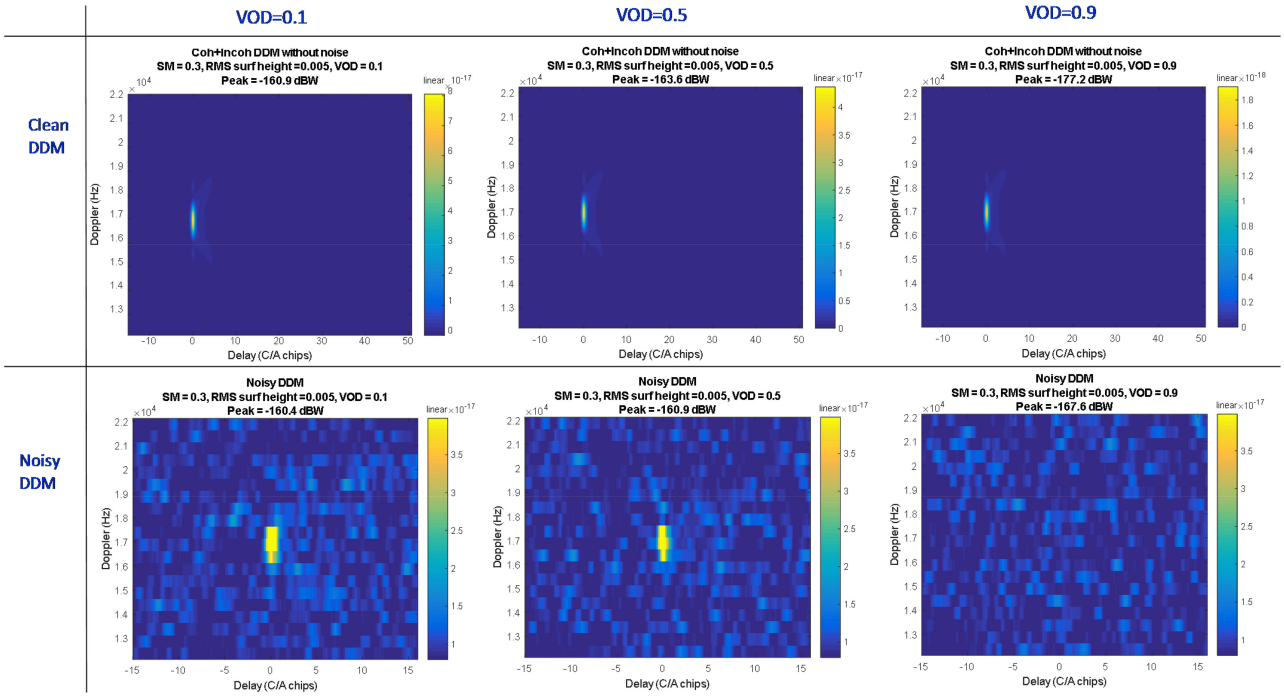

Fig. 24. Simulated clean and noisy DDMs with the effect of the VOD.

shows relatively higher DDM peaks as shown in the bottom panel of Fig. 15, because of water in part of the FOV.

D. Case 4: Amazon, High Vegetation, and In-Land Water

This location is quite interesting to study the impact of high vegetation and inland water. Amazon region is a tropical forest, having an immense amount of vegetation, and there is the Amazon river. Water places are high reflecting areas, so this river presents a chance to show the strong DDM peaks. Looking at the L1B Catalogue in TDS-1, there is a track that goes over this area on March 12, 2017, at H18. The satellite track is number 42. A simulation of 60 snapshots was performed over this area.

As seen in the track of this case (see Fig. 16), when the satellite track crosses over the river, the color changes to almost white (high DDM peak). Fig. 17 shows the conditions of the geophysical parameters over the region.

As it can be seen in Fig. 18, the DDM peak value starts very low corresponding to the heavily vegetated area. It rises as the specular point gets closer to the river, and it reaches a maximum value. Then, in the middle of the track, it drops due to the specular point leaving the river area, but soon it goes up again to peak on a nearby lake. Afterward, the DDM peak value drops down again as it leaves the water areas, and enters into the forest.

Fig. 19 shows examples of simulated and corresponding TDS-1 DDMs.

1) *Forest fraction*: Fig. 19 (top) shows DDMs for Amazon on its forest part at 4 s. The peak values are so low ($\sim$ -180 dBW) so that almost nothing is displayed on the snapshot.
2) *Amazon river*: Fig. 19 (bottom) corresponds to the specular point being on the river itself at 22 s, and it has a very high peak value (~ -162 dBW).

Note that the dynamic range of the signal ($\sim$20 dB) is also in line with CYGNSS data.[3]

Finally, Fig. 20 shows the DDM peak powers of the four cases. The peak powers of the dry region are quite low (around -170 dBW) as compared to the wet region. Specifically, the regions with water (inland or cost) show high DDM peak power (around -161 dBW). The heavy vegetation and forest drastically attenuate the power of the reflected signal, even making it smaller than the dry region. All these results are reasonable according to the geophysical conditions, and the observed and predicted dynamic ranges are in agreement.

V. Study on the Sensitivity With Homogeneous FOV

The benefit of the static mode of the simulator is that it is convenient to study the parameter impacts on the DDM. With a parameter-sweep simulation, the sensitivity of the geophysical parameters to the DDM can be efficiently studied. In this section, three main parameters are discussed: soil moisture, vegetation, and surface roughness.

A. Impact of Soil Moisture

An example of the simulated DDM with SM variation is shown in Fig. 21. As keeping the other parameters constant, the DDMs are simulated with SM change. Because of the homogeneous FOV condition, the shape of DDM is not much different. However, the power of DDM increases with SM. The slope of the curve can be calculated with two regimes: 43 dB/100% in the SM ranging [0–0.15] and 8.6 dB/100% in the range of

[3]Online. [Available]: https://www.nasa.gov/feature/goddard/2018/flood-detection-a-surprising-capability-of-microsatellites-mission

[0.15–0.45]. The slope in [0–0.45] is 17 dB/100%. Although the curve is not linear and the regimes are arbitrary, these values are in agreement with the experimental results in [3] and [38], which are 38 dB/100% for bare dry soils, and ∼9 dB/100% at a global scale.

B. Impact of Vegetation

An example of simulated DDM with respect to VOD is presented in Fig. 22. The vegetation effect is mainly the attenuation of the received power. From VOD = 0 to 0.6, the slope of the curve is – 11 dB, and if the VOD > 0.6 the vegetation attenuation drastically increases. It means that the received power reflected over the region with dense vegetation or forest is under the noise floor (see the clean and noisy DDM with the effect of the VOD in Fig. 24). In the case of VOD = 0.9, the feature of DDM is not found in the Noisy DDM because the peak power is around −177 dBW, which is much lower than the typical noise floor of GNSS-R instrument. The heavy vegetation effect is well illustrated in the case study of orbit progressing simulation in Section IV Amazon case.

C. Impact of Surface Roughness

An example of the simulated DDM with rms surface height variation is shown in Fig. 23.

As the surface becomes rougher, the signals are more scattered, which means more spread with less power. The curve is not linear. It can be divided into two regions arbitrarily, e.g. at 1.5 cm rms height. The slope of the decreasing curve is around –3.1 dB/cm from 0.5 to 1.5 cm, and −6.2 dB/cm from 1.5 to 3.5 cm, which are comparable to the result in [31]. The case of 3.5 cm rms height is very rough, and the peak values are around −178 dBW. In this case, the reflected signals are easily buried under the noise floor like in Fig. 24 and cannot be detected.

V. Conclusion

This article has presented an efficient simulator to study the impact of the geophysical parameters. The developed simulator allows studying the dependency of the DDMs for the individual parameters, such as the soil moisture and vegetation. Many other influential parameters can also be efficiently analyzed for their impacts on the DDM, e.g., the elevation angles, land cover, topography.

The simulator has been verified and validated using the TDS-1 data for four different cases. In the results, the peak values of the simulated DDM are well followed by the TDS-1 DDMs. The characteristics of the specific conditions of the FOV also appear well, e.g., dry and wet, desert and forest, inland water, and coast. In this article, the variation of DDM peak has also been tested.

References

[1] M. Unwin, P. Jales, J. Tye, C. Gommenginger, G. Foti, and J. Rosello, "Spaceborne GNSS-reflectometry on TechDemoSat-1: Early mission operations and exploitation," *IEEE J. Sel. Topics Appl. Earth Observ. Remote Sens.*, vol. 9, no. 10, pp. 4525–4539, Oct. 2016.

[2] C. Ruf *et al.*, "CYGNSS: Enabling the future of hurricane prediction [Remote Sensing Satellites]," *IEEE Geosci. Remote Sens. Mag.*, vol. 1, no. 2, pp. 52–67, Jun. 2013.

[3] A. Camps *et al.*, "Sensitivity of GNSS-R spaceborne observations to soil moisture and vegetation," *IEEE J. Sel. Topics Appl. Earth Observ. Remote Sens.*, vol. 9, no. 10, pp. 4730–4742, Oct. 2016.

[4] C. C. Chew and E. E. Small, "Soil moisture sensing using spaceborne GNSS reflections: Comparison of CYGNSS reflectivity to SMAP soil moisture," *Geophys. Res. Lett.*, vol. 45, no. 9, pp. 4049–4057, May 2018.

[5] H. Kim and V. Lakshmi, "Use of cyclone global navigation satellite system (CyGNSS) observations for estimation of soil moisture," *Geophys. Res. Lett.*, vol. 45, no. 16, pp. 8272–8282, Aug. 2018.

[6] M. M. Al-Khaldi, J. T. Johnson, A. J. O'Brien, A. Balenzano, and F. Mattia, "Time-series retrieval of soil moisture using CYGNSS," *IEEE Trans. Geosci. Remote Sens.*, vol. 57, no. 7, pp. 4322–4331, Jul. 2019.

[7] M. P. Clarizia, N. Pierdicca, and F. Costantini, "Analysis of CYGNSS data for soil moisture applications," *IEEE J. Sel. Top. Appl. Earth Obs. Remote Sens.*, vol. 12, no. 7, pp. 2227–2235, Jul. 2019.

[8] O. Eroglu, M. Kurum, D. Boyd, and A. C. Gurbuz, "High spatio-temporal resolution CYGNSS soil moisture estimates using artificial neural networks," *Remote Sens.*, vol. 11, no. 19, p. 2272, Sep. 2019.

[9] K. Jensen, K. McDonald, E. Podest, N. Rodriguez-Alvarez, V. Horna, and N. Steiner, "Assessing L-Band GNSS-reflectometry and imaging radar for detecting sub-canopy inundation dynamics in a tropicalwetlands complex," *Remote Sens.*, vol. 10, no. 9, p. 1431, 2018.

[10] E. Santi *et al.*, "Forest biomass estimate on local and global scales through GNSS reflectometry techniques," in *Proc. Int. Geosci. Remote Sens. Symp.*, 2019, pp. 8680–8683.

[11] C. Gerlein-Safdi and C. S. Ruf, "A CYGNSS-based algorithm for the detection of inland waterbodies," *Geophys. Res. Lett.*, vol. 46, no. 21, pp. 12065–12072, Nov. 2019.

[12] E. Loria *et al.*, "Analysis of wetland extent retrieval accuracy using Cygnss," in *Proc. Int. Geosci. Remote Sens. Symp.*, 2019, pp. 8684–8687.

[13] M. Morris, C. Chew, J. T. Reager, R. Shah, and C. Zuffada, "A novel approach to monitoring wetland dynamics using CYGNSS: Everglades case study," *Remote Sens. Environ.*, vol. 233, Nov. 2019, Art. no. 111417.

[14] J. D. Campbell and M. Moghaddam, "GNSS-R parameter sensitivities for soil moisture retrieval," in *Proc. 20th Int. Conf. Electromagn. Adv. Appl.*, 2018, pp. 609–612.

[15] N. Pierdicca, L. Guerriero, R. Giusto, M. Brogioni, and A. Egido, "SAVERS: A simulator of GNSS reflections from bare and vegetated soils," *IEEE Trans. Geosci. Remote Sens.*, vol. 52, no. 10, pp. 6542–6554, Oct. 2014.

[16] H. Park, A. Camps, D. Pascual, A. Alonso-Arroyo, J. Querol, and R. Onrubia, "Improvement of PAU/PARIS end-to-end performance simulator (P2EPS): Land scattering including topography," in *Proc. Int. Geosci. Remote Sens. Symp.*, Beijing, China, 2016, pp. 5607–5610.

[17] L. Dente, L. Guerriero, D. Comite, and N. Pierdicca, "Space-borne GNSS-R signal over a complex topography: Modelling and validation," *IEEE J. Sel. Topics Appl. Earth Observ. Remote Sens.*, vol. 13, pp. 1218–1233, Mar. 2020.

[18] H. Park *et al.*, "A Generic level 1 simulator for spaceborne GNSS-R missions and application to GEROS-ISS ocean reflectometry," *IEEE J. Sel. Topics Appl. Earth Observ. Remote Sens.*, vol. 10, no. 10, pp. 4645–4659, Oct. 2017.

[19] H. Carreno-Luengo, A. Amèzaga, D. Vidal, R. Olivé, J.-F. Munoz, and A. Camps, "First polarimetric GNSS-R measurements from a stratospheric flight over boreal forests," *Remote Sens.*, vol. 7, pp. 13120–13138, 2015.

[20] J. Wickert *et al.*, "GEROS-ISS: GNSS reflectometry, radio occultation, and scatterometry onboard the international space station," *IEEE J. Sel. Topics Appl. Earth Observ. Remote Sens.*, vol. 9, no. 10, pp. 4552–4581, Oct. 2016.

[21] A. Martinez-Vazquez, A. Camps, J. M. Lopez-Sanchez, M. Vall-llossera, and A. Monerris, "Numerical simulation of the full-polarimetric emissivity of vines and comparison with experimental data," *Remote Sens.*, vol. 1, pp. 300–317, 2009.

[22] A. Camps *et al.*, "Microwave imaging radiometers by aperture synthesis—performance simulator (Part 1): Radiative transfer module," *J. Imag.*, vol. 2, no. 2, p. 17, May 2016.

[23] Y.-C. Lin and K. Sarabandi, "Electromagnetic scattering model for a tree trunk above a tilted ground plane," *IEEE Trans. Geosci. Remote Sens.*, vol. 33, no. 4, pp. 1063–1070, Jul. 1995.

[24] P. Ferrazzoli, L. Guerriero, N. Pierdicca, and R. Rahmoune, "Forest biomass monitoring with GNSS-R: Theoretical simulations," *Adv. Space Res.*, vol. 47, no. 10, pp. 1823–1832, May 2011.

[25] M. Pardé, J. P. Wigneron, A. Chanzy, P. Waldteufel, Y. Kerr, and S. Huet, "Retrieving surface soil moisture over a wheat field: Comparison of different methods," *Remote Sens. Environ.*, vol. 87, pp. 334–344, 2003.
[26] M. Zribi *et al.*, "Performance of GNSS-R GLORI data for biomass estimation over the Landes forest," *Int. J. Appl. Earth Observ. Geoinf.*, vol. 74, pp. 150–158, Feb. 2019.
[27] Y. Y. Liu *et al.*, "Recent reversal in loss of global terrestrial biomass," *Nature Climate Change*, vol. 5, no. 5, pp. 470–474, May 2015.
[28] A. M. Balakhder, M. M. Al-Khaldi, and J. T. Johnson, "On the coherency of ocean and land surface specular scattering for GNSS-R and signals of opportunity systems," *IEEE Trans. Geosci. Remote Sens.*, vol. 57, no. 12, pp. 10426–10436, Dec. 2019.
[29] A. Camps, "Spatial Resolution in GNSS-R Under Coherent Scattering," *IEEE Geosci. Remote Sens. Lett.*, vol. 17, no. 1, pp. 32–36, Jan. 2020.
[30] D. Comite, F. Ticconi, L. Dente, L. Guerriero, and N. Pierdicca, "Bistatic coherent scattering from rough soils with application to GNSS reflectometry," *IEEE Trans. Geosci. Remote Sens.*, vol. 58, no. 1, pp. 612–625, Jan. 2020.
[31] W. Gu, H. Xu, and L. Tsang, "A numerical kirchhoff simulator for GNSS-R land applications," *Prog. Electromagn. Res.*, vol. 164, pp. 119–133, 2019.
[32] J. F. Marchan-Hernandez, A. Camps, N. Rodriguez-Alvarez, E. Valencia, X. Bosch-Lluis, and I. Ramos-Perez, "An efficient algorithm to the simulation of delay-doppler maps of reflected global navigation satellite system signals," *IEEE Trans. Geosci. Remote Sens.*, vol. 47, no. 8, pp. 2733–2740, Aug. 2009.
[33] D. Pascual, S. Member, H. Park, A. Camps, A. A. Arroyo, and R. Onrubia, "Simulation and analysis of GNSS-R composite waveforms using GPS and Galileo signals," *IEEE J. Sel. Topics Appl. Earth Observ. Remote Sens.*, vol. 7, no. 5, pp. 1461–1468, May 2014.
[34] L. Guerriero and D. Comite, "Simulations of spaceborne GNSS-R signal over mountain areas," in *Proc. IEEE Int. Geosci. Remote Sens. Symp.*, 2019, pp. 8362–8365.
[35] M. I. Skolnik, *Radar Handbook*, 2nd ed. New York, NY, USA: McGraw-Hill, 1990, ch. 25.
[36] J. T. Johnson, K. F. Warnick, and Peng Xu, "On the geometrical optics (Hagfors' Law) and physical optics approximations for scattering from exponentially correlated surfaces," *IEEE Trans. Geosci. Remote Sens.*, vol. 45, no. 8, pp. 2619–2629, Aug. 2007.
[37] H. Park *et al.*, "Retracking considerations in spaceborne GNSS-R altimetry," *GPS Solut.*, vol. 16, no. 4, pp. 507–518, Jan. 2012.
[38] A. Camps *et al.*, "Sensitivity of TDS-1 GNSS-R reflectivity to soil moisture: Global and regional differences and impact of different spatial scales," *Remote Sens.*, vol. 10, no. 11, p. 1856, Nov. 2018.

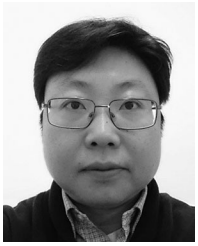

Hyuk Park (Senior Member, IEEE) was born in South Korea. He received the B.S. degree in mechanical engineering from the Korea Advanced Institute of Science and Technology, Daejeon, South Korea, in 2001 and the M.S. and Ph.D. degrees in information and mechatronics from Gwangju Institute of Science and Technology, Gwangju, South Korea, in 2003 and 2009, respectively.

In 2009, he was a Postdoctoral Researcher with the Remote Sensing Group, Polytechnic University of Catalonia (UPC), Barcelona, Spain. In 2011, he was a Grant Holder of National Research Foundation funded by the Korean Government. Since 2012, he has been a Research Associate with a Juan de la Cierva grant funded by the Spanish Ministry of Economy and Competitiveness. He is currently working with School of Telecommunications and Aerospace Engineering at Castelldefels (EETAC-UPC) as a Ramon y Cajal Fellow/Tenure-track Assistant Professor. He is also working with the Passive Remote Sensing Group, UPC, for satellite remote sensing for microwave radiometry and Global Navigation Satellite Systems reflectometry. His main research interests include remote sensing, particularly passive microwave remote sensing, including system design, modeling and simulation, image processing, and small satellite applications.

Adriano Camps (Fellow, IEEE) was born in Barcelona, Spain, in 1969. He received the degree in telecommunications engineering and the Ph.D. degree in telecommunications engineering from the Universitat Politècnica de Catalunya (UPC), Barcelona, Spain, in 1992 and 1996, respectively.

In 1991 to 1992, he was at the ENS des Télécommunications de Bretagne, France, with an Erasmus Fellowship. Since 1993, he has been with the Electromagnetics and Photonics Engineering Group, Department of Signal Theory and Communications, UPC, where he was first an Assistant Professor, an Associate Professor, in 1997, and a Full Professor since 2007. In 1999, he was on sabbatical leave with the Microwave Remote Sensing Laboratory, of the University of Massachusetts. Since 1993, he has been deeply involved with the European Space Agency SMOS Earth Explorer Mission, from the instrument and algorithmic points of view, performing field experiments, and since 2001, studying the use of GNSS-R techniques to perform the sea-state correction needed to retrieve salinity from L-band radiometric observations. His research interests are focused in microwave remote sensing, with special emphasis in microwave radiometry by aperture synthesis techniques and remote sensing using signals of opportunity (GNSS-R). He has published over 203 papers in peer-reviewed journals, six book chapters, one book, and more than 425 international conference presentations, holds 12 patents, and has advised 23 Ph.D. Thesis students (+8 on-going), and more than 120 final projects and M.Eng. Theses. According to Publish or Perish (Google Scholar) his publications have received more than 6347/9547 citations, and his h-index is 38 /47 according to Scopus/Google Scholar.Prof. Adriano Camps is currently the Scientific Coordinator of the CommSensLab "María de Maeztu" Excellence Research Unit, he co-led the Remote Sensing Lab (www.tsc.upc.edu/rs, www.tsc.upc.edu/prsblog) and co-leads the UPC NanoSat Lab (http://www.tsc.upc.edu/nanosatlab). He is the PI of the first four UPC nanosatellites: 3Cat-1, a 1U CubeSat with 7 small technology demonstrators and scientific payloads, 3Cat-2, a 6U CubeSat with the first dual-frequency dual-polarization GNSS-R payload, launched on August 15, 2016 using a Chinese LM-D2 rocket, 3Cat-4, a 1U Cubesat with a software defined radio to implement a microwave radiometer, a GNSS-Reflectomer, and an AIS receiver, and FSSCAT, a tandem mission formed by two 6U CubeSats, overall winner of the Copernicus masters competition 2017.

Dr. Camps was the Chair of uCal 2001, member of the IGARSS Technical Program Committee since 2002, IGARSS 2007 Technical Program Committee Co-chair, co-chair of GNSS-R '10, and co-chair of IGARSS 2020 and the 6th FFSS Workshop. He was Associate Editor of Radio Science, IEEE GEOSCIENCE AND REMOTE SENSING LETTERS, and he is currently an Associate Editor for the IEEE TRANSACTIONS ON GEOSCIENCE AND REMOTE SENSING. He was the President-Founder of the IEEE Geoscience and Remote Sensing Society (GRSS) Chapter at Spain. He has been the member of the IEEE Geoscience and Remote Sensing Society Administrative Committee, since 2002, where he has been the Newsletter Editor, the web editor, the Vice President of Information Resources, the Vice President of Meetings and Symposia, Executive Vice President, and in 2017 and 2018 President of the IEEE Geoscience and Remote Sensing Society. In 1993, he was the recipient of the Second National Award of University Studies; in 1997, the INDRA Award of the Spanish Association of Telecommunication Engineers to the best Ph.D. in Remote Sensing; in 1999 the Extraordinary Ph.D. Award at the Universitat Politècnica de Catalunya; in 2002, the Research Distinction of the Generalitat de Catalunya for contributions to microwave passive remote sensing; and in 2004, European Young Investigator Award, in 2009 and 2015 the ICREA Academia Award. In 2011, he was elevated to the grade of Fellow of the Institute of Electrical and Electronic Engineers for "For contributions to microwave remote sensing of land and sea surfaces." Finally, as a member of the Microwave Radiometry Group, UPC, he received in 2000, 2001, and 2004: the 1st Duran Farell and the Ciutat de Barcelona awards for Technology Transfer, and the "Salvà i Campillo" Award of the Professional Association of Telecommunication Engineers of Catalonia for the most innovative research project for MIRAS/SMOS related activities, and in 2010 the 7th Duran Farell award for Technological Research for the work on GNSS-R instrumentation and applications. In 2015, he and Mr. Querol was also the recipient of the European Satellite Navigation Competition Award-Barcelona Challenge for the FENIX system to detect and mitigate radio frequency interference in satellite navigation receivers, and in 2017 he was the winner of the Copernicus Masters ESA Sentinel Small Satellite Challenge and the Overall Winner of 2017 Copernicus Masters Competition.

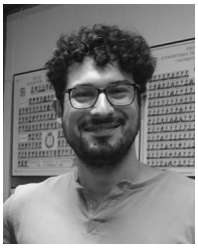

Jordi Castellvi received the university degree in telecommunications engineering from the Universitat Politècnica de Catalunya, Barcelona, Spain, in 2009. He is working in remote sensing, focused in soil moisture determination. The Ph.D. program is shared between the University of Catalonia and the Institut Cartogràfic i Geològic de Catalunya. The Ph.D. explores the feasibility to equip small satellites with L-band passive sensors to retrieve soil moisture. Field campaigns with airborne sensors, both microwave and optical, are being held to test the readiness and the possibility to increase spatial resolution through data fusion.

Jorge Muro was born in Spain. He received the university degree in aerospace engineering, in 2019 from the Politechnical University of Catalonia, Barcelona, Spain, where he is currently working toward the master's degree in aeronautical engineering.

His main interests include aeronautical world and specially the space industry.